Energy &
Environmental
Science

Resonant Energy Transfer Enhances Solar Thermal Desalination

Journal:	*Energy & Environmental Science*
Manuscript ID	EE-ART-10-2019-003256.R1
Article Type:	Paper
Date Submitted by the Author:	21-Jan-2020
Complete List of Authors:	Alabastri, Alessandro; Rice University, Dongare, Pratiksha; Rice University Neumann, Oara; Rice University Metz, Jordin; Rice University Adebiyi, Ifeoluwa; Rice University Nordlander, Peter; Rice University, Department of Physics and Astronomy Halas, Naomi; Rice University, Department of Electrical and Computer Engineering

Resonant Energy Transfer Enhances Solar Thermal Desalination

Alessandro Alabastri[a,b,c,#], Pratiksha D. Dongare[a,b,c,d,#], Oara Neumann[a,b,d], Jordin Metz[b,c,e], Ifeoluwa Adebiyi[d,f], Peter Nordlander[a,b,d,g,*], and Naomi J. Halas[a,b,d,f,g,*]

[a]Department of Electrical and Computer Engineering; [b]Laboratory for Nanophotonics,; [c]Nanosystems Engineering Research Center for Nanotechnology-Enabled Water Treatment (NEWT); [d]Applied Physics Graduate Program; [e]Department of Chemistry, Rice University, Houston, TX 77005; [f]Department of Engineering, Houston Community College, Houston, TX 77082; and [g]Department of Physics and Astronomy, Rice University, Houston, TX 77005

[#]Equal contribution

[*]Correspondence to: nordland@rice.edu (P.N.), halas@rice.edu (N.J.H.)

ABSTRACT

Evaporation-based solar thermal distillation is a promising approach for purifying high-salinity water, but the liquid-vapor phase transition inherent to this process makes it intrinsically energy intensive. Here we show that the exchange of heat between the distilled and input water can fulfill a resonance condition, resulting in dramatic increases in fresh water production. Large gains (500%) in distilled water are accomplished by coupling nanophotonics-enabled solar membrane distillation with dynamic thermal recovery, achieved by controlling input flow rates as a function of incident light intensity. The resonance condition, achieved for the circulating heat flux between the distillate and feed, allows the system to behave in an entirely new way, as a desalination oscillator. The resonant oscillator concept introduced here is universal and can be applied to other systems such as thermal energy storage or solar-powered chemical reactors.

BROADER CONTEXT

With increasing scarcity of invaluable fresh water resource on Earth, evaporation based solar driven phase change processes are promising for providing fresh water by evaporating alternative saline water sources like seawater and brackish reservoirs. These solar thermal desalination processes can also help reduce the water waste from existing desalination plants and industrial produced and processed water. The amount of water purified with solar thermal desalination is limited by the energy consumption for the liquid to vapor phase change process. In this work, we demonstrate how the phase change vaporization energy can be recovered and reused to heat input saline feed in the solar thermal desalination with the help of a resonant thermal recovery system. The combined thermal desalination oscillator (TDO) system results in optimal purified water production by matching the saline feed and purified distillate flows for a given system size and losses depending on incident light intensity. A 1 m^2 TDO system can produce more than 20 litres of purified water per day. Resonant dynamic thermal recovery will enable optimal utilization of available energy sources like sunlight and waste heat for thermal desalination bringing them significantly closer to real life applications.

INTRODUCTION

The lack of reliable access to drinkable water for billions of people around the world and the increasing use of water for industrial processes make fresh water availability a challenge of global importance[1, 2]. While utilizing alternative sources like seawater, brackish and processed water is a potential solution, current water treatment methods face the major limitation of low fresh water recovery from such highly saline sources[3-5]. High concentrations of dissolved solids make filtration techniques ineffective and pressure-based approaches impractical[6, 7]. A potential solution to the clean water crisis is off-grid solar thermal desalination technology, developed with modular designs combining lightweight and cost-effective materials[8-25]. These qualities make solar thermal desalination a promising approach for high-salinity water purification, with potential applications in areas lacking access to conventional electrical power.

The main limitation of any evaporation-based desalination process is its intrinsically low thermodynamic efficiency due to its reliance on energy-intensive phase change[26, 27]. Recovering the heat of vaporization is therefore an obvious path towards increasing efficiency. Here we examine the coupling between nanophotonics-enabled solar membrane distillation[8] (NESMD) and a dynamic heat recovery (HX) system. We show how these two processes can be combined to recover much of the heat of condensation from the distillate, reusing it to pre-heat the feed. Increased distilled water rates due to heat recovery have been observed for conventional membrane distillation[28-33]. However, here we show that this coupled system can behave as a resonant thermal desalination oscillator (TDO), resulting in dramatic increases in distillate output at its resonance condition. Tuning the feed and distillate flows as a function of illumination intensity is found to be critical for achieving optimized oscillator condition, which also depends on module size and thermal losses. In a highly compact dynamic TDO system, we see a 500% increase in distillate flux on resonance compared to a nonresonant system, demonstrating 1.1 $kg/m^2{\cdot}h$ fresh water generation and collection under 475 W/m^2 irradiation. We analyze the principal mechanisms of the TDO system, explain its limitations, and propose potential future designs. Additionally, we show how an intensity-dependent dynamic input flow control can maintain system optimization throughout an entire day of use. A simple model to theoretically analyze the key principles behind resonant energy transfer shows how such systems can be related to more general resonant phenomena.

In its simplest form, NESMD features two countercurrent flows, saline feed (F) and purified distillate (D) separated by a hydrophobic, light-absorbing membrane (Fig. 1a, b). Sunlight is converted into heat on the feed side through photothermal heating by light-absorbing nanoparticles[8] embedded in the membrane's porous surface layer. The induced temperature gradient across the membrane results in water evaporation on the feed side and condensation on the distillate side. The continuous, localized heating at the feed/membrane interface due to incident sunlight makes NESMD size scalable and avoids temperature polarization, overcoming two main drawbacks of conventional membrane distillation[8]. In NESMD, the hydrophobic membrane is ~100 μm thick, and the top ~2-10 μm membrane layer is embedded with highly light-absorptive carbon black (CB) nanoparticles[34]. Once generated, the distillate is brought into thermal contact with the saline feed for heat exchange (Fig. 1a, b). Thermal contact is achieved through a copper or aluminum sheet incorporated into the flow structure. In practice, folding the HX below the NESMD module avoids increasing the system footprint, which would allow a high density of NESMD modules to be positioned within a compact area.

EXPERIMENTAL SETUP

The experiment was performed using a 10.2 cm × 20.3 cm NESMD module with a 10.2 cm × 40.6 cm inline HX (Fig. 1b) with 2 mm water channels on both sides. The system details of the individual components are reported in our previous work[34]. To study the effect of heat exchange in reaching the resonance condition of the system, we tried to minimize the variation of external parameters, such as incident light intensity and temperature. The NESMD was thus illuminated with an LED lamp (FAISHILAN 200W LED Flood Light, 1000W Halogen Equivalent Outdoor Work Lights, IP66 Waterproof with US-3 Plug & Switch, 20000Lm, 6500K) at a distance resulting in an intensity of ~475 W/m^2. The feed and distillate input temperatures were maintained equal and constant at 25 ˚C with a water bath (SoCal Biomed). This water bath temperature is referred to as the ambient temperature. The external temperature was ~ 20 ˚C. In all theoretical modeling, the input ambient temperature for feed and distillate was set to 25 ˚C and external sink temperature was set to 20 ˚C. Variable velocity peristaltic pumps (Cole-Parmer Peristaltic Pump; 0.4 to 85 mL/min, 12VDC/115VAC UX-73160-32) were used to circulate 1 weight% saline feed and deionized distillate at the top and bottom of the membrane respectively. The light absorbing membrane mounted in the NESMD unit is fabricated by spray coating polyvinylidene difluoride (PVDF) membranes with a light absorbing layer of carbon black (Cabot Corporation) nanoparticles. 10.2 cm × 40.6 cm heat exchanger included ~500 μm thick aluminum sheet for the heat exchange. Our current experimental setup utilizes input feed water at a relatively low 1% (10,000 TDS) salinity. However, as shown by Swaminathan et. al.[33], large solute contents in the feed channel can have a sensitive impact on the flow rate optimization and should be taken into account to maximize heat recovery.

RESULTS AND DISCUSSION

Thermal desalination oscillator performance

Maintaining the feed flow (Q_F) constant at 6.5 mL/min, a clear resonant behavior can be observed by varying the distillate flow achieving a maximum purified water flux of ~1.1 kg/($m^2\cdot h$) as shown in Fig. 1c. The measured experimental flux for the coupled system is shown in Fig. 1c (blue diamonds). The blue shaded region corresponds to the simulated purified water flux for these experimental conditions (see Supplementary Note 1, Supplementary Figs. 1-3 for details). The width of the simulation curve reflects the variations in the penetration depth of the CB coating (2-10 microns). The experimentally measured (magenta triangles) and calculated (magenta shaded region) flux for the bare NESMD system is also shown. In the coupled system, when the distillate flow is much faster ($Q_D >> Q_F$) or much slower ($Q_D << Q_F$) than the feed, the distillate flux is significantly lower than the flux at the resonant condition. The calculated power transferred from distillate to feed in the HX region is shown in Fig. 1d and peaks at matched feed and distillate velocities.

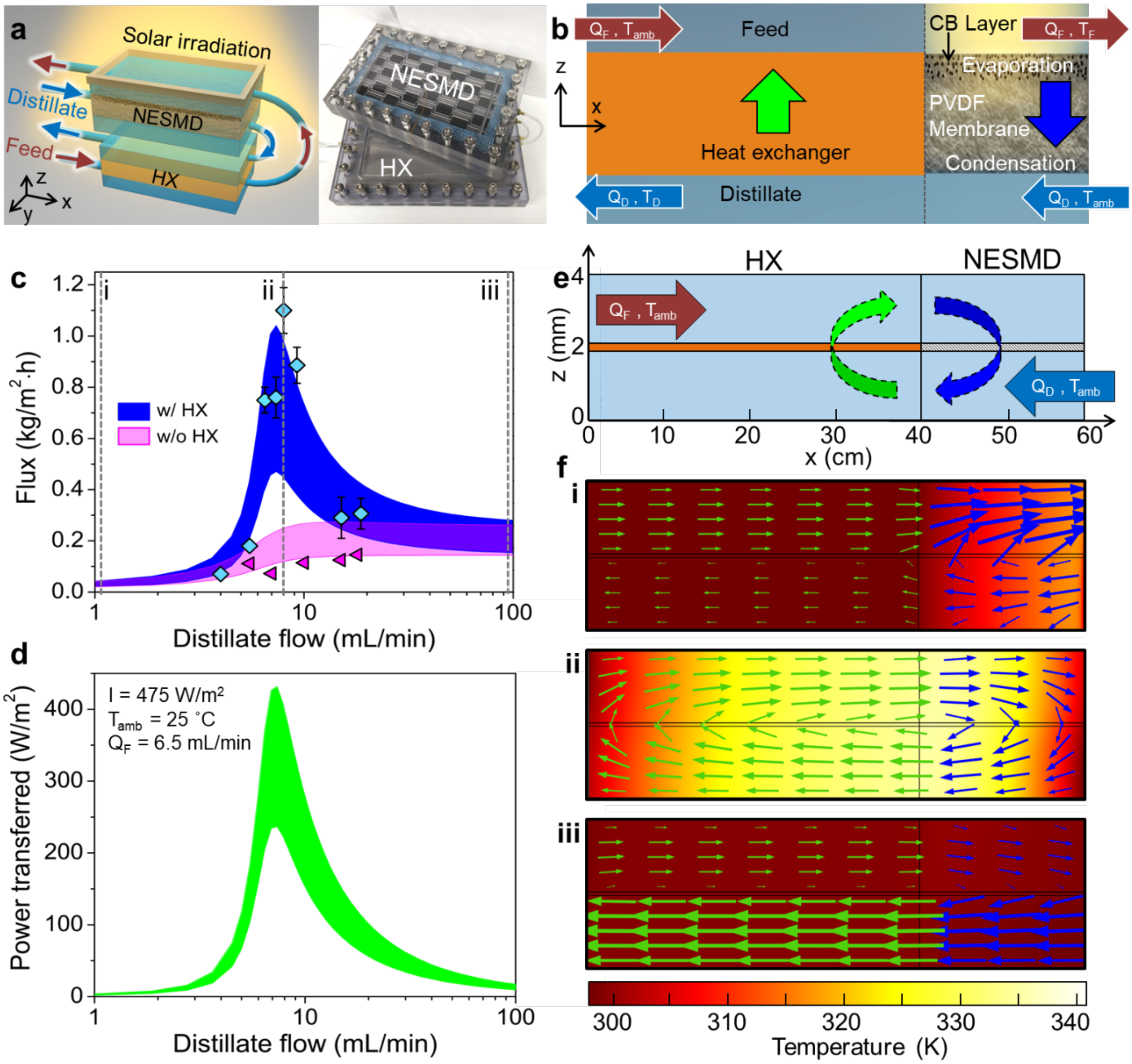

Fig. 1| Flux and power transfer in thermal desalination oscillator (TDO) for different distillate flow. **a**, Saline feed is in thermal contact with the outgoing distillate through a HX. The feed is further heated from the photothermal membrane. The digital image of the 10.2 cm × 20.3 cm NESMD with underlying 10.2 cm × 20.3 cm HX is also shown. **b**, Schematic of unfolded system with 10.2 cm × 20.3 cm NESMD and 10.2 cm × 40.6 cm inline HX. **c**, Calculated flux through 10.2 cm × 20.3 cm NESMD with (blue curve) and without (magenta curve) 10.2 cm × 40.6 cm inline HX for varying distillate flow at fixed feed flow of 6.5 mL/min. The uncertainty is due to the variation (2-10 µm) in CB thickness. Measured flux with HX (blue diamonds) and without HX (magenta triangles). **d**, Calculated power transferred from distillate to feed for the device in **c**. **e**, 2D schematic of the device: water is represented by the blue area, HX by orange, and the light absorbing membrane by grey. **f**, Total heat flux vector field (arrows- blue: NESMD and green: HX) in the TDO system at fixed feed flow of 6.5 mL/min and distillate flow of (i) 1 mL/min ($Q_D << Q_F$), (ii) 7.4 mL/min ($Q_D \sim Q_F$), and (iii) 100 mL/min ($Q_D >> Q_F$).

To further understand the origin of the resonant behavior, we consider a two-dimensional schematic of the TDO system (Fig. 1e). The total (conduction and convection) heat flux vector field maps in the regimes of $Q_D<<Q_F$, $Q_D\sim Q_F$ and $Q_D>>Q_F$ are shown in Fig. 1f (i), (ii), and (iii) respectively. The three regimes yield very different heat fluxes and temperature distributions. A well-defined circular heat flux appears in Fig. 1f (ii) when $Q_D\sim Q_F$, the resonant condition. A more detailed analysis is presented in Supplementary Fig 4. For $Q_D<<Q_F$ (Fig. 1f(i) and Supplementary Fig 4), the feed receives heat from the membrane but quickly loses it through its outlet. The maximum temperature difference occurs at the feed outlet, where the incoming distillate temperature is close to 25 °C. In the rest of the device, the slow distillate receives heat from the counter-flowing feed, resulting in a slightly negative temperature difference (Supplementary Fig 4a). A negative $\Delta T(x)$ results in 'back evaporation', *i.e.* evaporation from the distillate to the feed (Supplementary Fig 4b). This explains why the blue energy flux arrows in the NESMD region in Fig. 1f(i) point from distillate to feed. For $Q_D\sim Q_F$, the feed first increases its temperature along *x*, absorbing heat from the distillate through conduction. In the membrane region with positive $\Delta T(x)$, heat is transferred to the distillate through water evaporation (Supplementary Fig 4c-d). The hot distillate exiting the membrane region exchanges heat with the feed and its temperature is reduced. This process is maximized as the heat starts circulating in the system, as shown by the flux arrows in Fig. 1f(ii). Heat is cycled back and forth between the feed and distillate and this resonant effect is the origin of the dramatically increased water flux. For $Q_D>>Q_F$, the slower feed receives more heat from the light absorbing layer. The faster distillate reduces the interaction time between feed and distillate, maintaining an overall positive temperature gradient across the membrane (Supplementary Fig 4e-f). This results in heat flow from feed to distillate in the form of purified water flux, as shown in Fig. 1f(iii). While the distillate collects heat through condensation, the low interaction time limits heat exchange and the heat is lost as the distillate exits the HX (Fig. 1f(iii), green arrows).

While the concept of resonance in desalination or heat recovery systems is new, we believe that its use appropriately describes the process described in this work. When flow rates are matched (resonant condition) the energy stored and its decay time are maximized due to overall loss minimization, a hallmark of oscillating systems at resonance. This effect is due to the heat fluxes that alternate (oscillate) between feed and distillate (see Fig. 1f,ii). Interestingly, as shown by Lin et. al.[28] and Swaminathan et. al.[32, 33], the same matching condition is found in conventional membrane distillation systems with external heating sources. The key difference is that the modules described in this work include the (light-induced) heating source internally, creating a compact region where thermal energy is stored and cycled to drive the desalination. In Supplementary Note 4 we show in detail how it is possible to analytically calculate, for a simplified but fundamentally equivalent case, the energy decay time, highlighting the similarities with more common time-driven harmonic oscillators."

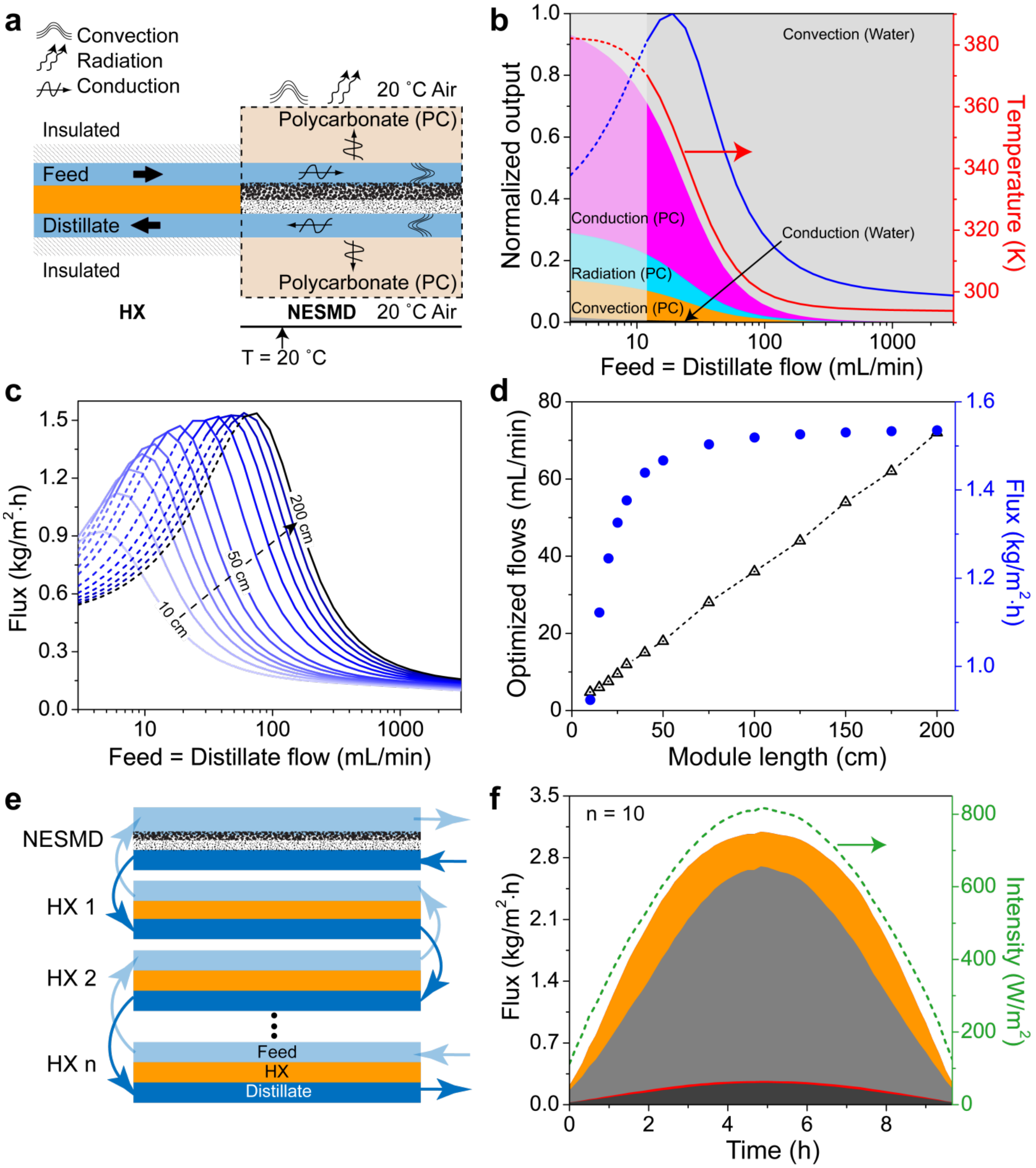

Fig. 2| Purified water production enhancement for TDO system with size scale up. a, Schematic of the TDO system showing different heat loss mechanisms in the two parts of the coupled system. **b**, Conduction, convection and radiation losses in the polycarbonate window layer and water channels in a 10.3 cm × 50 cm NESMD connected to a 10.3 cm × 50 cm HX normalized to input solar power at 20 °C under 1 Sun illumination (1 kW/m^2). The normalized distillate flux is shown in blue. **c**, Distillate flux from a 10.3 cm wide NESMD module with length ranging from 10 cm to 200 cm with heat exchanger of the same size, for equal feed and distillate flow rates. Dashed lines indicate flux when maximum temperature in the system is above the boiling point of water. **d**, Optimal matched flow rate values (left y-axis, black) and corresponding flux rate (right y-axis, blue) for different module sizes. **e**, Schematic of a stacked TDO system. **f**, Comparison of flux production from NESMD with 10 HX layers during a 9 hour day with (orange) and without (grey) dynamic control (left axis). Flux rates for the same system without HX layers with (red) and without (dark grey) dynamic control. Solar intensity variation in green (right axis).

Dynamic thermal recovery with system size, losses and intensity

The performance of NESMD systems has been predicted to improve with increasing module size. Here we analyze the scalability for the TDO system. A schematic of a coupled system with equal membrane and conductor lengths is depicted in Fig. 2a. The relevant loss mechanisms are convection and conduction through the feed and distillate water flows, conduction through the polycarbonate (PC) window to the environment, and convection/radiation from the top PC surface. The relative weights of each loss channel normalized to input solar power as a function of flow (Supplementary Note 1) are shown in Fig. 2b.

The dependence of flux rates on the feed and distillate flows is shown in Fig. 2c. The dashed curves correspond to configurations where the maximum temperature in the system (T_{max}) is higher than the boiling point of water (T_B) (Supplementary Fig. 5). Configurations exhibiting temperatures in this range would not be operational, but it is informative to include them here since they provide context for understanding system optimization. The two main features observed in Fig. 2c are: (i) each curve exhibits a peak in flux for a given pair of matched feed and distillate flows and (ii), the peak flux value increases with size up to a particular length (~50 cm) before saturation at ~1.5 kg/m^{2}·h.

The flux rate increases from its low value at lower flow rates because all three loss mechanisms, conduction, convection and radiation, in PC are reduced as the feed flow rate is increased (Fig. 2c). This was illustrated in Fig. 2b, which shows the relative losses from the NESMD region normalized to the input heat source from absorbed sunlight. At higher flow rates, the dominant loss is convection, mostly by the feed and distillate themselves. The optimal trade-off between external losses and heat recirculation occurs for a flow of ~20 mL/min and module length of ~50 cm, corresponding to a maximum fresh water flux rate of ~1.5 kg/(m^{2}·h) (Fig. 2c). Although the resonant oscillator behavior is optimized with a sacrifice of scale-up, the possibility of maximizing fresh water flux in finite size modules enables portable or modular systems with unprecedented performance and efficiency for distributed household settings, for example.

The saturation value of the distillate flux rate as system size is increased depends on the balance between accumulated thermal energy, flow velocities, and external losses. More extended modules benefit from larger light-absorbing areas, but require faster flows and longer heat exchangers. The optimal matched flows for different system sizes (Fig 2c) are shown in Fig. 2d. Matched flows increase with system size because additional convective cooling is required to avoid boiling and maintain an optimal temperature profile to maximize the flux.

To maintain resonance and optimum distillate flux values, the flow rates must be tuned dynamically, throughout a typical day, as the solar radiation varies. We consider a 50 cm insulated NESMD system with limited radiation losses (with a low-emissivity coating of $\epsilon = 0.01$ in the infrared). The idea is to configure an efficient, folded and stacked structure (Fig. 2e) with n HX layers. For the typical solar intensities in Alamogordo, NM, (green dashed curve in Fig. 2f), we analyze TDO performance using n = 10 HX layers throughout the day. For each input light intensity, we selected the optimal pair of matched flows (Supplementary Fig. 6) to obtain optimal water production (orange area in Fig. 2f). We compare water flux production for dynamic flow change with intensity (orange) with the flux from the device with flow values optimized for 1 Sun (grey) in Fig. 2f. By integrating the flux rates over the entire day, dynamical flow rate control yields a total output of 20.5 L/(m^2·day) compared to 15.9 L/(m^2·day) for fixed flow (grey), a net 29% gain. The yield from an NESMD system without HX would be much smaller: 1.7 L/(m^2·day) with dynamic flow rate control, and 1.5 L/(m^2·day) with no flow rate control. The specific energy consumption (i.e. the energy consumed to generate 1 cubic meter of purified water) of the dynamic heat recovery system is 276.8 kWh..

The flux rate dependence on n (from 1 to 10) for different incident intensities, I, (from 0.1 to 1 Sun) is shown in Supplementary Fig. 7. Flux rates increase with intensity for a given n because more power is harvested by the light absorbing nanoparticles. The flux also increases with increasing n because the distillate can transfer more heat back to the feed through the longer path length provided by more HX layers. To achieve larger fluxes at higher intensities, the matched flows need to increase in order to maintain the temperature below the boiling point of water. While higher intensities give larger fluxes, efficiency starts dropping above a certain intensity (Supplementary Fig. 8). The reason is subtle: for a given intensity, the typical flux vs. matched flows curve has a shape of the type shown in Fig. 2c, featuring a peak flow rate and lower performance for larger or smaller flows. However, the constraint $T_{max} < T_B$ pushes the $T_{max} \sim T_B$ edge away from the peak, toward higher matched flow regions. This translates into a sub-optimal efficiency.

The optimal efficiency conditions also depend on losses. So far we have assumed a small combined heat transfer coefficient $h_{HX} = 0.01\, W/(m^2K)$ since the HX is not exposed to the environment and can be well insulated. We have also performed an analysis of the impact of HX losses on the system performance. Interestingly, we have found that dynamic flow rate control can also be applied to mitigate losses (Supplementary Note 2, Supplementary Fig. 9). In future designs, the real-time dynamic flow control should also take into account the varying feed salinity and the decreasing/increasing feed/distillate flows (due to the transfer of evaporated water between the two channels), as suggested in Swaminathan et. al.[33], to ensure an even more accurate heat recovery optimization.

Theoretical analysis of heat flux dynamics across resonance

The concept of resonant heat exchange is quite general and applicable to other thermal processes. Let us examine a simple model where two adjacent channels, feed (F) and distillate (D) of length L and thickness w, are separated by a thin thermal conductor and flow in counter-current mode upon entering the system at a temperature T_{amb} (Fig. 3a). Water in the F and D channels flows at rates $Q_F = Au_F$ and $Q_D = Au_D$ respectively, where u_F and u_D denote the velocities and A the cross-sectional area. The water density is ρ, and heat capacity is c. Both flows are insulated from the environment and a constant heat source I_s (W/m^2) is placed between the channels. F and D can exchange heat $I_{F\leftrightarrows D}$ (along z) through an effective heat transfer coefficient h_{eff}. Phase changes in the fluid are not considered, and all parameters are assumed temperature independent. We further assume that heat is carried by the flows (advection), neglecting conductive heat transfer parallel to flow directions. This assumption is reasonable in the case of large Peclet (Pe) numbers[35] $(Pe \gg 1$ in our case). Heat can leave the system through the F and D outlets. These assumptions allow characterizing the interaction between F and D as two coupled analytically solvable 1D systems (Supplementary Note 3, 4 and 5).

In Fig. 3b, we plot $I_{F\rightarrow D}$ (blue lines) and $I_{D\rightarrow F}$ (green lines) normalized to the input heat source I_s , for different u_F values and dimensionless parameters $\gamma_D = \frac{h_{eff}L}{cw\rho}\frac{1}{u_D}$ which conveniently includes all the system parameters and can be tuned simply by changing u_D. A peak in thermal exchange is reached when $\gamma_D \approx \gamma_F$ $(i.e.\ u_D \approx u_F)$ where $I_{F\rightarrow D} \approx I_{D\rightarrow F}$. Here heat circulates between F and D (Fig. 3a) leading to an accumulation of thermal energy. In mathematical terms, when $u_D \rightarrow u_F$ the system becomes symmetric for 180° rotations of the xz plane and heat fluxes must be equal in magnitude and with opposite directions. The curves do not overlap at different flow velocities ($\gamma_D \gg \gamma_F$ or $\gamma_D \ll \gamma_F$) due to the lack of mirror symmetry with respect to z (the flow velocities have opposite signs). It can also be understood in simple physical terms. If $\gamma_D \ll \gamma_F$, the distillate flow is much faster than the feed flow, and the whole D channel is close to T_{amb}. Therefore $I_{F\rightarrow D}$ is positive and $I_{D\rightarrow F}$ is negative. Vice versa, when $\gamma_D \gg \gamma_F$, heat transfers are reversed.

It is possible to describe the flow-dependent heat transfer $I_{F\leftrightarrows D}$ as a Lorentzian (Supplementary Fig. 10) without fitting parameters. Lorentzian responses are typical of many oscillating phenomena, reinforcing our description of this coupled system as one having a resonance. The overlap is exact at $\gamma_D = \gamma_F$ where we have:

$$I_{F\rightarrow D} \cong I_{D\rightarrow F} = \frac{1}{2} I_s \gamma, \text{with } \gamma = \gamma_D = \gamma_F \; (i.e.\; u_D = u_F)$$

This phenomenon has analogies with many other resonant oscillator systems (*e.g.,* laser cavities, plasmonic nanoparticles, ring resonators) where an external source couples to a system (*e.g.,* light incident on a metallic nanoparticle) which stores energy (*e.g.,* electromagnetic energy) before releasing or dissipating the input power (*e.g.,* scattered radiation or heat). In our case, the system (one of the channels) is driven by a flow rate (the opposite, heated channel), the stored energy is thermal, and the coupled and the released powers are heat fluxes.

Besides establishing the resonant condition, γ plays the role of the heat transfer 'enhancement' (I/I_s) between the channels. With $\gamma \propto L/u$, longer channels (larger L) will obtain stronger coupling for high-velocity flows. This general picture is relevant for the specifics of the TDO system, with I_s representing heat generated by the CB nanoparticles and $I_{F\rightarrow D}$, $I_{D\rightarrow F}$ representing evaporation-condensation and recovered heat fluxes respectively. A predicted $\frac{I_{F\rightarrow D}}{I_s} > 1$ translates to a thermal desalination efficiency $\eta = \frac{I_{evap}}{I_s} > 1$ where $I_{evap} = H_{evap}F$, H_{evap} (J/kg) is the water enthalpy of vaporization and F (kg/(m^{2}h)) represents the distilled flux rate. An efficiency larger than one can be associated with the gained output ratio (GOR) which quantifies how condensation heat is reused for further distillation[36]. Considering the obtained flux rates with and without HX, we can estimate a GOR ~ 5 for the experimental results reported in Fig. 1 and a maximum GOR ~ 12 for the n = 10 stacked configuration (Supplementary Fig. 11). The dynamic control also ensures a relatively large GOR > 8 for all sunlight intensities typically achieved during a day. Additional details are in Supplementary Note 6.

The analytical model can be extended to explain the effect of losses, expressed by the peaks shown in Fig. 2c. The model assumes now matched flows $(u_D = u_F)$ and an effective loss coefficient g_{eff} which transfers heat to the environment (see Supplementary Note 5, Supplementary Figs. 12 and 13 for details). The exchanged heat flux enhancement dependence on matched flows for different module sizes is shown in Fig. 3c. Consistent with full numerical calculations (Fig. 2c), a maximum heat transfer exists for a specific value of matched flows and such value depends on the channel length (Fig. 2d).

To visualize the oscillating behavior of the coupled channels, we have performed 2D numerical simulations for the system in Fig. 3a where the heated flows are considered laminar and coupled with thermal transport. In Fig. 3d-f we plot the temperature maps (colors, normalized to the maximum temperature in each case) of the coupled F and D channels far from resonance (Fig. 3d: $Q_F\,/Q_D\ =\ 10$, Fig. 3e: $Q_F\,/Q_D\ =\ 0.1$) and close to resonance (Fig. 3f: $Q_F\,/Q_D\ =\ 1$). To track the heat flux dynamics, we show trajectories (black lines) of massless probes inserted close to the origin and propagated by the heat flux field until they leave the system (black dots). Far from resonance, probes are transported to the F or D channel outlets following relatively direct paths (Fig. 3d, e). At resonance, the probe circulates from F to D and vice-versa multiple times before exiting the channels (Fig. 3e). This dynamics well describes the ability of the system to re-utilize heat. The cases of slower resonant flows are shown in Supplementary Fig. 14.

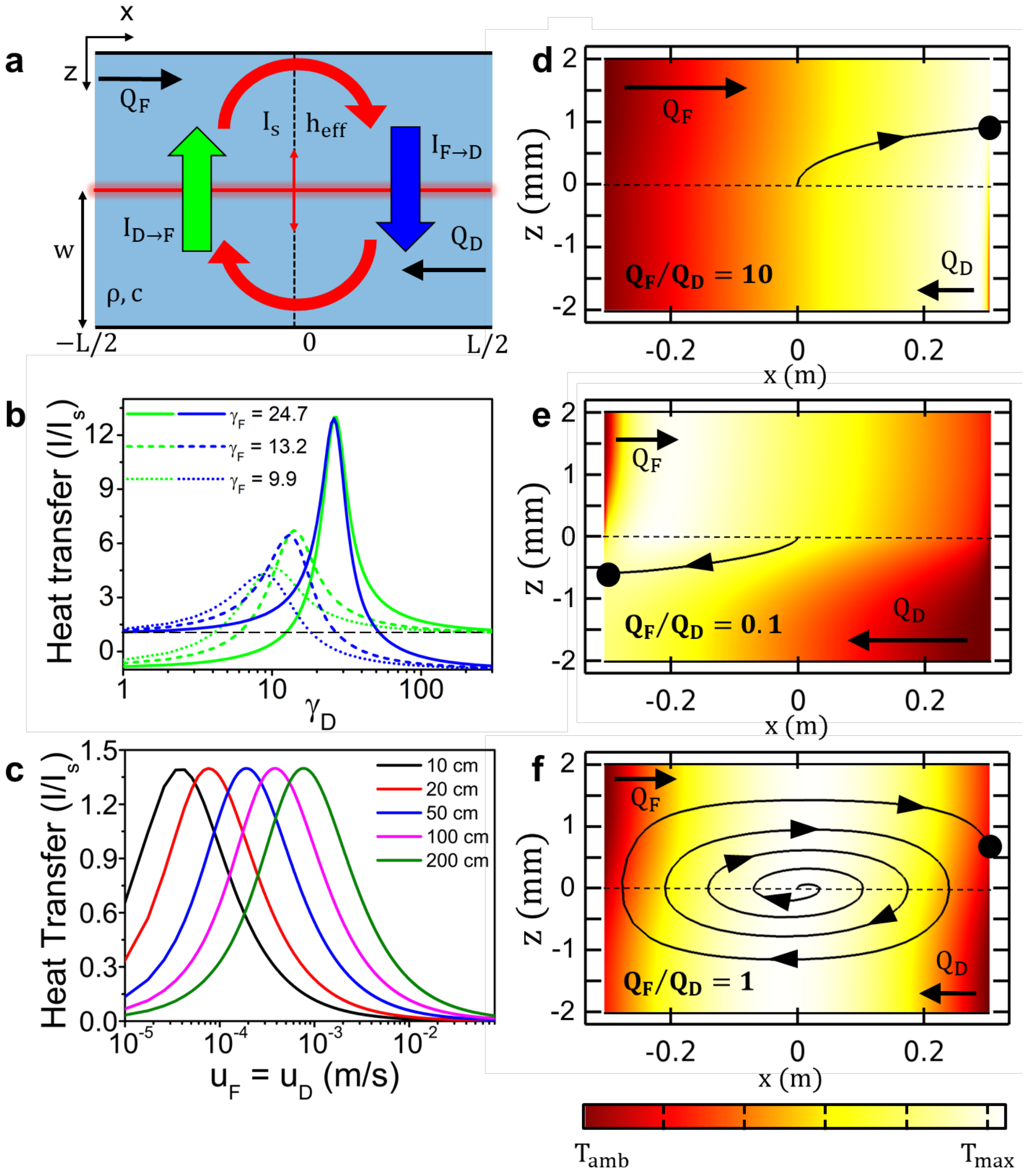

Fig. 3| Illustration of the resonant heat transfer concept. a, Two interacting channels of length L and thickness w. Two counter-current flows, Q_F and Q_D, are separated by a heat conductor which also serves as planar heat source I_s (W/m^2). The flows transport heat through advection along x and heat exchange along z through an effective heat transfer coefficient h_{eff} (W/m^2/K) which accounts for both water and conductor thermal properties. The net heat transfers $I_{F\to D}$ and $I_{D\to F}$ are calculated in the regions $[0 - L/2]$ and $[-L/2 - 0]$ respectively. The system is assumed thermally insulated. Heat exits the system through the outlets. Density and specific heat of the flows (water) are ρ and c respectively. Red arrows represent the heat flows for near resonant condition. **b**, Heat transfer enhancements (normalized to I$_s$) for $I_{F\to D}$ (solid, blue) and $I_{D\to F}$ (solid, green) as functions of Q_D with fixed Q_F and h_{eff}= 200 W/m^2/K, L = 24 in, c = 4.18 kJ/kg/K, ρ = 1 g/cm^3. Flow rates Q_F are 8, 15 and 20 mL/min for a cross section of thickness w = 2 mm and width d = 4 in. The horizontal dashed line is $I/I_s = 1$. **c**, Heat transfer enhancements (normalized to I$_s$) for $I_{F\to D}$ as functions of $u_D = u_D$ for varying system lengths of 10 cm, 20 cm, 50 cm, 100 cm and 200 cm. **d**, Calculated temperature map (colors) for Q_F = 20 mL/min and Q_D = 2 mL/min. The black curve is the space-time trajectory of a massless probe, inserted at (0,0) until it leaves one of the channels. **e**, Same as **d** but Q_F = 20 mL/min and Q_D = 200 mL/min. **f**, Same as **d** and **e** with $Q_F = Q_D$ = 20 mL/min.

CONCLUSIONS

We have shown that a resonant oscillator condition can occur when a solar thermal distillation system is combined with heat exchange between matched distillate and feed flows, and can be optimized for a given input light intensity. Fresh water fluxes can be dramatically increased by this resonant behavior: in our experiments, a fivefold flux increase (from ~0.2 $kg/m^{2}\cdot h$ to ~1 $kg/m^{2}\cdot h$) was achieved in a small system. For optimal performance throughout an entire day, dynamic control of the input flow as a function of solar illumination intensity is required to support this high-output behavior. This insight can open the door to the design of new compact modular systems that efficiently balance input energy with system losses to achieve highly efficient performance for general types of solar- or heat- driven processes.

ACKNOWLEDGEMENTS

The authors acknowledge help and support from staff members Randall Shaw, Roberto Granados and Dan Lucero at Bureau of Reclamation's Brackish Groundwater National Desalination Research Facility (BGNDRF) during the outdoor solar experiments conducted at Alamogordo, New Mexico. The authors acknowledge help from Eliberto Batres and Atilla E. Thomazy with fabricating the NESMD devices. Ifeoluwa Adebiyi acknowledges support from Nanosystems Engineering Research Center for Nanotechnology-enabled Water Treatment (NEWT) through research experience for community college students (REU) program. **Funding**: This work was funded by NSF Award EEC-1449500, Air Force Office of Scientific Research Grant FA9550-15-1-0022, Robert A. Welch Foundation Grants C-1220 (NJH) and C-1222 (PN), and Peter M. and Ruth L. Nicholas Fellowship (ON).

DECLARATION OF INTERESTS

P.D., A.A., O.N., P.N. and N.J.H. are co-inventors on a provisional patent relating to the presented research.

References

1. M. M. Mekonnen and A. Y. Hoekstra, *Science Advances*, 2016, **2**, e1500323.
2. D. J. Lampert, H. Cai and A. Elgowainy, *Energy & Environmental Science*, 2016, **9**, 787-802.
3. I. G. Wenten and Khoiruddin, *Desalination*, 2016, **391**, 112-125.
4. M. Elimelech and W. A. Phillip, *Science*, 2011, **333**, 712-717.

5. J. R. Werber, C. O. Osuji and M. Elimelech, *Nature Reviews Materials*, 2016, **1**, 16018.
6. L. F. Greenlee, D. F. Lawler, B. D. Freeman, B. Marrot and P. Moulin, *Water Research*, 2009, **43**, 2317-2348.
7. N. Ghaffour, T. M. Missimer and G. L. Amy, *Desalination*, 2013, **309**, 197-207.
8. P. D. Dongare, A. Alabastri, S. Pedersen, K. R. Zodrow, N. J. Hogan, O. Neumann, J. Wu, T. Wang, A. Deshmukh, M. Elimelech, Q. Li, P. Nordlander and N. J. Halas, *Proceedings of the National Academy of Sciences*, 2017, **114**, 6936-6941.
9. E. Chiavazzo, M. Morciano, F. Viglino, M. Fasano and P. Asinari, *Nature Sustainability*, 2018, **1**, 763-772.
10. Y. Liu, S. Yu, R. Feng, A. Bernard, Y. Liu, Y. Zhang, H. Duan, W. Shang, P. Tao, C. Song and T. Deng, *Advanced Materials*, 2015, **27**, 2768-2774.
11. O. Neumann, A. S. Urban, J. Day, S. Lal, P. Nordlander and N. J. Halas, *ACS Nano*, 2013, **7**, 42-49.
12. N. Xu, X. Hu, W. Xu, X. Li, L. Zhou, S. Zhu and J. Zhu, *Advanced Materials*, 2017, **29**, 1606762.
13. F. Zhao, X. Zhou, Y. Shi, X. Qian, M. Alexander, X. Zhao, S. Mendez, R. Yang, L. Qu and G. Yu, *Nature Nanotechnology*, 2018, **13**, 489-495.
14. S. Ishii, R. P. Sugavaneshwar and T. Nagao, *The Journal of Physical Chemistry C*, 2016, **120**, 2343-2348.
15. Y. Ito, Y. Tanabe, J. Han, T. Fujita, K. Tanigaki and M. Chen, *Advanced Materials*, 2015, **27**, 4302-4307.
16. G. Xue, K. Liu, Q. Chen, P. Yang, J. Li, T. Ding, J. Duan, B. Qi and J. Zhou, *ACS Applied Materials & Interfaces*, 2017, **9**, 15052-15057.
17. L. Zhou, Y. Tan, D. Ji, B. Zhu, P. Zhang, J. Xu, Q. Gan, Z. Yu and J. Zhu, *Sci Adv*, 2016, **2**, e1501227.
18. L. Zhou, Y. Tan, J. Wang, W. Xu, Y. Yuan, W. Cai, S. Zhu and J. Zhu, *Nature Photonics*, 2016, **10**, 393.
19. G. Ni, G. Li, Svetlana V. Boriskina, H. Li, W. Yang, T. Zhang and G. Chen, *Nature Energy*, 2016, **1**, 16126.
20. M. Gao, L. Zhu, C. K. Peh and G. W. Ho, *Energy & Environmental Science*, 2019, **12**, 841-864.
21. Y. Xia, Q. Hou, H. Jubaer, Y. Li, Y. Kang, S. Yuan, H. Liu, M. W. Woo, L. Zhang, L. Gao, H. Wang and X. Zhang, *Energy & Environmental Science*, 2019, **12**, 1840-1847.
22. S. He, C. Chen, Y. Kuang, R. Mi, Y. Liu, Y. Pei, W. Kong, W. Gan, H. Xie, E. Hitz, C. Jia, X. Chen, A. Gong, J. Liao, J. Li, Z. J. Ren, B. Yang, S. Das and L. Hu, *Energy & Environmental Science*, 2019, **12**, 1558-1567.
23. G. Xue, Q. Chen, S. Lin, J. Duan, P. Yang, K. Liu, J. Li and J. Zhou, *Global challenges.*, 2018, **2**.
24. W. Wang, Y. Shi, C. Zhang, S. Hong, L. Shi, J. Chang, R. Li, Y. Jin, C. Ong, S. Zhuo and P. Wang, *Nature Communications*, 2019, **10**, 3012.
25. A. Politano, P. Argurio, G. D. Profio, V. Sanna, A. Cupolillo, S. Chakraborty, H. A. Arafat and E. Curcio, *Advanced materials.*, 2017, **29**.
26. A. Faghri and Y. Zhang, in *Transport Phenomena in Multiphase Systems*, eds. A. Faghri and Y. Zhang, Academic Press, Boston, 2006, DOI: https://doi.org/10.1016/B978-0-12-370610-2.50007-6, pp. 107-176.
27. A. Al-Karaghouli and L. L. Kazmerski, *Renewable and Sustainable Energy Reviews*, 2013, **24**, 343-356.
28. S. Lin, N. Y. Yip and M. Elimelech, *Journal of Membrane Science*, 2014, **453**, 498-515.
29. A. Najib, J. Orfi, E. Ali and J. Saleh, *Desalination*, 2019, **466**, 52-67.
30. R. Long, X. Lai, Z. Liu and W. Liu, *Energy*, 2018, **148**, 1060-1068.
31. G. Guan, X. Yang, R. Wang and A. G. Fane, *Desalination*, 2015, **366**, 80-93.
32. J. Swaminathan, H. W. Chung, D. M. Warsinger and J. H. Lienhard V, *Applied Energy*, 2016, **184**, 491-505.

33. J. Swaminathan, H. W. Chung, D. M. Warsinger and J. H. Lienhard V, *Desalination*, 2016, **383**, 53-59.
34. P. D. Dongare, A. Alabastri, O. Neumann, P. Nordlander and N. J. Halas, *Proceedings of the National Academy of Sciences*, 2019, **116**, 13182-13187.
35. R. M. H. Merks, A. G. Hoekstra and P. M. A. Sloot, *Journal of Computational Physics*, 2002, **183**, 563-576.
36. Z. Wang, T. Horseman, A. P. Straub, N. Y. Yip, D. Li, M. Elimelech and S. Lin, *Science Advances*, 2019, **5**, eaax0763.